Environ. Sci. Technol. **2004**, *38,* 4396−4408

Intercorrelations among Degree of Geochemical Alterations, Physicochemical Properties, and Organic Sorption Equilibria of Kerogen

CHEN YANG,† WEILIN HUANG,*,‡ BAOHUA XIAO,‡ ZHIQIANG YU,† PING'AN PENG,† JIAMO FU,† AND GUOYING SHENG†

State Key Laboratory of Organic Geochemistry, Guangzhou Institute of Geochemistry, Chinese Academy of Sciences, Wushan, Guangzhou 510640, People's Republic of China, and Department of Environmental Sciences, Rutgers University, New Brunswick, New Jersey 08901-8551

Recent studies reported that kerogen is an important natural organic material dominating sorption of relatively hydrophobic organic contaminants (HOCs) by topsoils and river sediments collected from industrialized regions. Due to its chemical and structural heterogeneity, kerogen is expected to exhibit a spectrum of sorptive phenomena for HOCs. The goal of this study is to establish correlations between heterogeneous physicochemical properties of kerogen and its sorptive characteristics for HOCs. In this study, we simulated diagenetic alterations under laboratory conditions by thermally treating a low-grade lignite at 200, 250, 300, 350, 400, 450, and 500 °C, yielding a series of type III kerogen samples having the same parental material but different maturations and physicochemical properties. The treated samples and the original lignite were systematically characterized using different methods and were used as the sorbents for sorption equilibrium study. The results of characterization revealed that black carbon or char was formed at 450 °C or above and that, as the treatment temperature (*T*) increases, both O/C and H/C atomic ratios decrease whereas aromaticity and reflectance index increase. The sorption and desorption isotherms measured for 1,3,5-trichlorobenzene and phenanthrene are nonlinear and hysteretic. The nonlinearity and apparent desorption hysteresis increase as a function of *T* and correlate well with rigidity and aromaticity of the organic matrix. The sorption capacity for each sorbate increases initially as *T* increases, reaches a maximum at 300−350 °C, and then decreases rapidly as *T* increases beyond 350 °C. This study suggests that the highly heterogeneous kerogen-based coal materials may have varied elemental compositions, functionalities, and matrix rigidity and that they could play major roles in the isotherm nonlinearity and the apparent sorption−desorption hysteresis exhibited by soils and sediments.

* Corresponding author phone: (732)932-7928; fax: (732)932-8644; e-mail: whuang@envsci.rutgers.edu.

† Chinese Academy of Sciences.

‡ Rutgers University.

Introduction

Sorption is a major process controlling chemical and biological reactivities of relatively hydrophobic organic contaminants (HOCs) in surface aquatic and groundwater systems. Quantitative estimation and mechanistic interpretation of the sorptive interactions between HOCs and soils and sediments is key to implementations of many physical, chemical, and biological process-based strategies for remedy of HOC-contaminated subsurface systems. Prior studies showed that sorption and desorption by soils and sediments are dominated by the interactions of HOCs with soil organic matter (SOM) (*1*−*3*) and that such interactions highly depend on the content and type of SOM (*1*−*12*). The widely accepted classic sorption theories are predicated on a hypothesis that humic acids may be the major SOM component dominating the overall HOC sorption processes in soils (*1*−*3*). However, several recent studies revealed that kerogen and black carbon materials are important SOM components in soils and sediments collected from urbanized and industrialized areas (*11*−*19*) and that these materials, instead of humic acids, may dominate the overall HOC sorption by soils (*11*, *12*, *15*−*18*, *20*−*26*). Since kerogen and black carbon are chemically and structurally very different from humic acids (*6*, *7*, *9*, *11*, *14*), their interactions with HOCs may be mechanistically and phenomenologically different from the classic sorption theories such as the linear partition theorem (*7*, *11*−*13*, *15*−*32*).

Sorption by black carbon or charred materials, for example, has been shown in recent studies to follow site-limiting adsorption process on external and internal surfaces (*12*, *15*−*24*, *30*−*32*). Depending upon the particle sizes and origins, black carbon possesses organic carbon-normalized sorption capacity 1 or 2 orders of magnitude higher than humic acids at fixed aqueous concentrations of a given HOC (*12*, *15*−*23*, *29*−*32*).

Kerogen, the nonextractable component of coal, is widely utilized in various civil and industrial activities. HOC sorption by kerogen is less understood likely because kerogen is chemically and structurally much more heterogeneous. Unlike black carbon, which has aromatic rings as the dominant carbon structure, kerogen has both aromatic and aliphatic structure moieties with several oxygen- and nitrogen-containing functional groups as minor structural fragments (*9*, *25*, *33*−*36*). The content of each structural unit in kerogen depends on both the source material from which kerogen was originated and the geochemical alterations it had undergone. According to the geochemistry literature (*33*−*35*), kerogen can be classified to type I, II, and III (Figure 1) corresponding respectively to the source materials of fatty acid-rich animal and microorganism remnants, pollens and cuticles, and plant tissues and cellulose. Each type of kerogen consists of a spectrum of organic materials that have undergone a different degrees of geochemical alterations ranging from early diagenesis to late diagenesis (production of crude oil), catagenesis (production of natural gas), and metagenesis or graphitization, depending upon the conditions of temperature, pressure, and duration under which kerogen had been buried in the subsurface. Black carbon or charred materials are categorized in coal petrology as type IV kerogen, which is likely independent of source materials and is located in the narrow region of the late catagenesis and metagenesis (Figure 1). The highly heterogeneous properties of kerogen due to different degrees of geological alterations and different source materials should lead to greatly varied HOC sorption phenomena with possibly different mechanisms. Selection of representative samples

10.1021/es0350381 CCC: $27.50 © 2004 American Chemical Society
Published on Web 07/20/2004

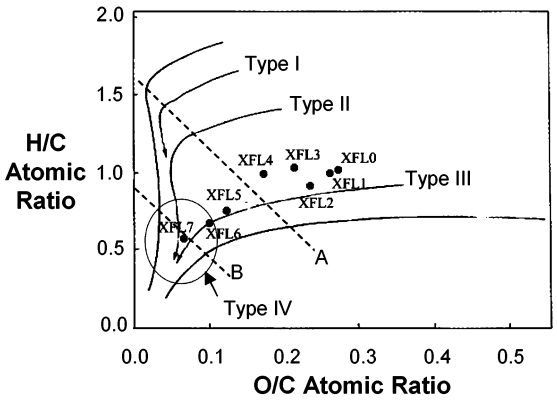

FIGURE 1. van Krevelen plot showing the evolution pathways of three types of kerogen as a function of geochemical alterations. The two dashed lines, A and B, represent the approximate boundaries of diagenesis−catagenesis and catagenesis−metagenesis, respectively. Filled circles are the eight kerogen samples examined in this study.

is key to capturing the entire spectrum of sorptive phenomena and to elucidating underlying mechanisms.

This study examined the impact of the degree of geochemical alterations on HOC sorption by kerogen. Unlike prior studies that selected kerogen samples originated naturally from different source materials under varied geological conditions (*6*), this study employed a thermal simulation procedure to yield a series of variously artificially matured kerogen materials from a low-grade and geochemically less altered lignite. The advantage of using the simulated materials from the same parental material as the sorbents is that their heterogeneous properties should be depended primarily upon the simulated geochemical conditions whereas the impact of source materials should be consistent. The differences of sorption properties among the sorbents can be related mainly to the maturation of the kerogen materials instead of the differences of source materials. The thermal simulation procedure was widely used in geochemical literature for mimicking geological alterations of kerogen under laboratory conditions. We systematically characterized the simulated kerogen materials and their parental lignite using different physical, chemical, and spectroscopic techniques. Sorption isotherms were measured using phenanthrene and 1,3,5-trichlorobenzene as the representative HOCs. We hypothesized that sorption capacity and isotherm nonlinearity depend on such properties as elemental composition, functionality, aromaticity, and matrix rigidity of kerogen. The purpose of this study is to establish intercorrelations among sorption characteristics, degree of geochemical alteration, and physicochemical properties of the kerogen materials, and our goal is to elucidate the mechanisms for sorption by kerogen.

Experimental Section

Lignite Sample and Its Thermal Treatment. The lignite sample was collected from Xianfeng Coal Mine, Kunming, Yunnan Province of China. It was selected as the original organic material in this study because its dominant organic matrix is a type III kerogen with mild diagenetic alterations. Because of its less matured nature, thermal simulations can generate a set of organic samples with varied physicochemical properties. The sample was ground, and the fraction with sizes of <0.5 mm was divided to eight subsamples, seven of which were sealed in Pyrex glass ampules (100 mm L × 15 mm i.d.), and an opening of about 0.1 mm was left to allow oxygen to diffuse into and react with the organic materials at the designated temperatures. Ampules were heated in a muffle furnace at 25 °C/min to designated temperatures of 200 °C (XFL1), 250 °C (XFL2), 300 °C (XFL3), 350 °C (XFL4), 400 °C (XFL5), 450 °C (XFL6), and 500 °C (XFL7) for 72 h. This thermal treatment procedure has been well-established in organic geochemistry literature (*34*, *37*−*39*) and has been widely used for mimicking diagenesis and catagenesis of kerogen (*37*−*41*). After thermal treatment, the subsamples, along with the untreated original subsample (XFL0), were Soxhlet extracted with a solvent mixture of methanol:acetone: methyl benzene at volumetric ratios of 2:3:5 for 7−30 d until the solvents became relatively colorless. The extracted materials were vacuum-dried at 60 °C for 10 d to eliminate the organic solvents. The eight samples (XFL0−7) were ground and the fractions of 63−100 μm were retained for this study.

Sorbent Characterization. The major physical and chemical properties of the eight samples were characterized systematically. The carbon, hydrogen, oxygen, and nitrogen contents were determined with a high-temperature combustion technique on Heraeus elemental analyzer (CHN−O−RAPID). Their specific surface areas (SSA) were measured using the N_2-adsorption /desorption data collected for each sample at the liquid-N_2 temperature (ASAP-1000, Micromeritics). Black carbon contents were quantified with the wet chemical oxidation method of Song et al. (*14*) [i.e., demineralization in HF + HCl acids followed by oxidative digestion in an aqueous solution of dichromate/sulfuric acid ($K_2Cr_2O_7$ (0.1 M) + H_2SO_4 (~2 M)) at 55 ± 1 °C for 60 h]. After completion of oxidative treatment, the residual solids were obtained by centrifugation, rinsed with Milli-Q water, and oven-dried at 80 °C for 72 h. The dried solids were then weighed and analyzed for TOC. The BC content was calculated from the mass and TOC contents of each sample before and after treatment (*14*).

The organic petrographic examinations were conducted with an optical microscopy (Leitz MPV-3) in both reflecting and fluorescent modes; the fluorescence was induced by blue light at excitation wavelength of 546 nm. The reflectance of organic matrix, an optical parameter indicative of the hardness or rigidity of kerogen, was measured with standard procedures of coal petrology (*35*). The polished sections used for the petrographic examinations were prepared by spreading organic particles on porcelain slides and cementing the particles with low-fluorescent 502 mucilage glue. The slides were then sliced, and the surfaces were polished.

Solid-state ^{13}C nuclear magnetic resonance (NMR) spectra were obtained on a Bruker DRX-400 NMR spectrometer at a ^{13}C frequency of 100 MHz and a magic-angle-spinning (MAS) rate of 6.0 kHz. The solid samples were filled in a 5-mm diameter ZrO_2 rotor with a Kel-F cap. A 1.2-s recycle time and a 1.0-ms contact time were used.

FTIR spectra were obtained on a Perkin-Elmer 1725 X FTIR spectrometer equipped with an automatic data acquisition system. The sample pellets used were prepared by pressing a mixture of 1 mg of well-ground sample and 60 mg infrared-grade KBr. The morphology and sizes of organic particles were measured on a scanning electron microscopy (SEM) (Hitachi S-3500N SEM with Oxford Link ISIS 300 EDS (energy-dispersive X-ray spectrometer)).

HOC Solutes. The two organic solutes, phenanthrene (log K_{OW} = 4.57, S_W = 1.12 mg/L) and 1,3,5-trichlorobenzene (TCB) (log K_{OW} = 4.02, S_W = 5.36 mg/L), were employed as the solutes in this study. They are commonly found in contaminated aquatic systems and have been widely used in recent sorption studies (e.g., refs *9*−*11*). They were obtained in spectrophotometric grade (98%) from Aldrich Chemical Co., Inc. and used as received.

Primary stock solutions were prepared by dissolving appropriate amount of each chemical in HPLC-grade methanol, and a series of stock solutions of various concentrations were prepared by sequential dilution of the primary stock

TABLE 1. Sorbent Properties

sample	treatment temp (°C)	weight loss (wt %)	TOC loss (wt %)	elemental composition C	N	H	O	ash content (wt %)	O/C	H/C	BC (wt %)	BET-N_2 SSA (m^2/g)	reflectance index R^0 (%)
XFL0	–[a]	–	–	60.4		4.76	23.0	2.58	0.29	0.95	–	4.50	0.31
XFL1	200	16.4	10.3	62.3	2.12	4.85	22.7	2.74	0.27	0.93	–	6.04	0.38
XFL2	250	20.8	13.4	64.3	2.05	4.71	20.9	2.86	0.24	0.88	–	2.69	0.46
XFL3	300	26.2	17.1	65.4	1.09	5.50	19.6	3.04	0.22	1.01	–	3.79	0.59
XFL4	350	34.8	24.3	69.9	2.47	5.53	16.3	3.51	0.18	0.95	–	4.71	0.86
XFL5	400	41.4	31.0	75.0	2.72	4.64	13.3	3.86	0.13	0.74	–	7.69	1.42
XFL6	450	46.2	36.0	77.9	2.70	4.46	10.1	4.21	0.10	0.69	76.9	10.7	2.07
XFL7	500	49.2	39.8	80.9	2.66	3.67	7.30	4.54	0.07	0.54	80.0	17.1	2.61

[a] Not detected.

solutions. All stock solutions were stored at 4 °C in glass bottles sealed with Teflon-lined tops. Initial aqueous solutions were prepared by mixing a background solution and a desired volume of a stock solution in a volumetric flask. The background solution consisted of 0.005 M $CaCl_2$ as a major mineral constituent, 100 mg/L NaN_3 to control biological activity, and 5 mg/L $NaHCO_3$ to buffer at pH 7.0. In all initial aqueous solutions methanol content was <0.2 vol %, at which level methanol has no measurable effect on sorption (*42*). The solute concentrations of initial solutions were analyzed with a procedure described below.

Sorption and Desorption Experiments. Completely mixed batch reactor (CMBR) systems were employed for sorption and desorption equilibrium experiments at room temperature (22 ± 0.5 °C). Flame-sealed glass ampules (25 and 60 mL, Wheaton) were used as the CMBRs. The experiments consisted of preliminary tests and final equilibrium tests. The preliminary tests were designed to determine the time required for attaining apparent sorption equilibrium and an appropriate sorbent-to-solution ratio for each sorbent-solution system; the optimal ratio should yield a 30−70% reduction in aqueous-phase solute concentration in each reactor at the completion of final sorption experiment. The final tests were conducted for acquisition of the equilibrium data reported here. Solid−solution contact times of 42 d were used for attainment of apparent sorption and desorption equilibria. Desorption was measured with a single-cycle decant−refill technique. The procedures for measuring sorption and desorption equilibria described in refs *9* and *43* were followed. In brief, CMBRs filled with aqueous sorbate solutions and fixed amount of sorbents were sealed in a propane flame and mixed continuously in a shaker preset at 125 rpm. After 42 d, the reactors were set upright for 2 d to allow the particles to settle. They were opened in the propane flame and weighed. An aliquot of supernatant was withdrawn from each reactor and mixed with a fixed volume of methanol in a 5-mL vial capped with Teflon-lined tops; this mixture was used for analysis of aqueous-phase solute concentrations. After the supernatant in each reactor was emptied with a pipet, the reactor was weighed, refilled with solute-free background solution, weighed, flame-sealed, and placed in the shaker for desorption of the sorbate from the solid. After 42 d of mixing, the reactors were set upright for 2 d. It was broken open, and the supernatant was withdrawn from each reactor and mixed with methanol for analysis of the solution-phase sorbate concentration.

In each set of experiments, 10 reactors containing no sorbent prepared in a way similar to the reactors containing sorbents were run simultaneously to assess loss of solutes to reactor components during sorption and desorption tests. The average concentration of the control reactors was within 98−102% of the initial concentration. No correction for solute loss was made during reduction of sorption data.

Solute concentrations of the initial aqueous solutions were analyzed on a reversed-phase HPLC (Hewlett-Packard model 1100, ODS, 5 μm, 2.1 × 250 mm C-18 column) with both diode array UV and fluorescence detector. TCB was analyzed using the UV detector set at 205 nm wavelength. Phenanthrene was quantified using the UV detector set at 250 nm wavelength for high solute concentration ranges and the fluorescence detector set at 250 nm excitation wavelength and 364 nm emission wavelengths for low concentration ranges. External methanol solution standards were used to establish linear calibration curves for both UV and fluorescence detectors. The eluting solvent used was a mixture of acetonitrile (90%) and water (10%). The detection limits of the methods for phenanthrene and TCB are 0.5 and 2 μg/L, respectively. The solid-phase solute concentrations were computed based on the mass balance of the solute between the two phases.

Results and Discussion

Chemical Characteristics. Table 1 lists the treatment temperature, weight loss, elemental composition, ash content, O/C and H/C elemental ratios, BC content, BET-N_2 specific surface area, and the reflectivity index (R^0) for each sorbent. It shows that the loss of mass due to partial oxidation of organic matter increases from 16.4% for XFL1 to 49.2% for XFL7 as the treatment temperature (T) increases from 200 to 500 °C. The thermal alterations of the lignite are well represented by changes of chemical compositions and other physicochemical and macromolecular properties. It is apparent from Table 1 that TOC content increases from 60.4% for XFL0 to 62.3% for XFL1 and to 80.9% for XFL7 whereas the oxygen content decreases from 23.0% to 22.7% and to 7.3%, respectively. Organic nitrogen and hydrogen contents remain relatively constant, but the ash content increases, suggesting that the inorganic matter is relatively stable under the thermal treatment conditions. A plot of H/C vs O/C atomic ratios on the van Krevenlen diagram (Figure 1) indicates that the elemental composition of the thermally treated materials follows the expected trend of maturation of type III kerogen materials as a function of alterations. The H/C atomic ratio remains relatively constant at 0.88−1.01 for XFL0−4 and then decreases dramatically to 0.74 for XFL-5 and to 0.54 for XFL7, suggesting that aliphatic carbons be eliminated from the organic matrix at T ~350 °C and that the remaining organic matrixes become more aromatic, consistent with the reported observations for naturally occurring type III kerogen (*34*). The O/C atomic ratio also remains relatively constant at 0.22−0.29 for XFL0−3 and then decreases to 0.18 for XFL4 and to 0.08 for XFL7, suggesting that oxygen-containing functional groups were substantially removed from the organic matter matrix at temperatures near 250−300 °C. This is consistent with organic geochemistry literature that decarboxylation of kerogen matrixes is the predominant diagenetic alterations of kerogen at temperature below 300 °C whereas cracking of aliphatic carbon chains dominates above 300 °C. The good agreement shown in Figure 1 on the chemical evolution of type III kerogen between our thermal simulation and the

natural aging process indicates that lignin-based organic materials undergo similar degradation reactions under both thermal simulation and natural diagenetic conditions. The thermal degradation rates are apparently much faster than the natural diagenesis under which pressure is relatively higher (40−100 bar) and H_2O, instead of O_2, is present.

BC contents listed in Table 1 are about 80 wt % for XFL 6 and XFL7 and not measurable for the samples treated at $T \leq 400$ °C, indicating that the organic matrixes of XFL6 and XFL7 are predominantly black carbon or char and that the optimal T for the formation of BC is >400 °C. The lower than 100% of the BC content determined for the two sorbents is likely due to both sample loss and partial oxidation of BC particles during BC measurement (*14*).

Petrographic Examinations. The change of organic matter matrix as a function of T can be clearly observed under petrographic microscopy. Under the reflecting mode, two types of organic macerals identified include an unaltered and less altered vitrinite maceral with gray colored and smooth, homogeneous surfaces (Figure 2a,b) and a charred semifusinite or fusinite maceral with bright color and rough, porous surfaces (Figure 2c.d). Vitrinite is the dominant maceral in XFL0 and XFL1−5. Fusinite, which is found occasionally in both XFL4 (Figure 2b) and XFL5, is predominant in both XFL6 (Figure 2c) and XFL7 (Figure 2d).

Table 1 lists the reflectance of vitrinite, R^0, an indicator of matrix rigidity and maturation degree of organic matter under different diagenetic conditions. The greater R^0 value correlates to more rigid and condensed kerogen matrix. According to Table 1, the measured R^0 value increases slightly from 0.31% for XFL0 to 0.59% for XFL3 and 0.86% for XFL4 and then increases sharply to 1.42% for XFL5 to 2.61%, the highest reflectance, for XFL7. This consists of a complete spectrum of products of geochemical alterations from early diagenesis ($R^0 \leq 0.5-0.6\%$) to early diagenesis ($R^0 \leq 1.1-1.2\%$), catagenesis ($R^0 \leq 2.4\%$), and to metagenesis ($R^0 > 2.4\%$) (*34*, *35*). Fairly linear relationships between the measured R^0 values and the O/C and H/C atomic ratios are shown in Figure 3, suggesting that the organic matrixes become more rigid and matured after removal of branched aliphatic chains and oxygen-containing functionalities as T increases.

Under the fluorescent microscopy, the intensity and color spectrum of the visible light emitted by organic particles in response to the UV excitation are functions of kerogen maturation. At low maturation levels, XFL0 (Figure 2e) exhibits yellow color near the edges of particles. As T increases, the fluorescence color at the edges of particles changes to orange (XFL1, Figure 2f), brown (XFL3, Figure 2g), and colorlessness (XFL4, Figure 2h), indicating a gradual maturation of organic matter due to thermal alterations. These phenomena are consistent with the observations for typical natural organic matter having similar diagenetic alteration histories (*34*, *35*).

Scanning Electron Microscopy (SEM) Analysis. SEM images are presented in Figure 4a−d, which indicates transition of relatively smooth and laminated surfaces for XFL0 (Figure 4a) and slightly altered surfaces for particles (XFL2) treated at lower T (Figure 4b) to porous and rough surfaces for particles (XFL5 and XFL7) treated at higher T due to more severe thermal alterations (Figure 4c,d). It is possible that the porous structures found for XFL5−7 were probably due to charring or elimination of volatile moieties within the organic matrixes and that the roughness of the surfaces are indicative of rigidity or brittleness of the organic matrixes since the particles examined had been ground.

Specific Surface Areas. Table 1 shows that the BET N_2-gas SSA decreases initially and then increases as T increases from 200 to 500 °C. The initial decrease of SSA is likely caused by expanding process, a physical process in which aliphatic

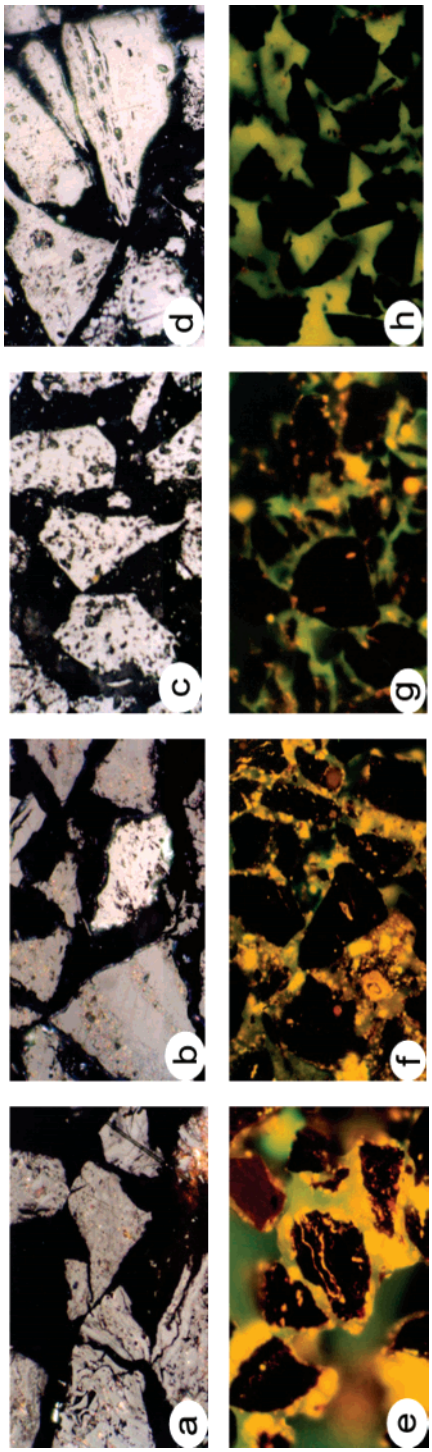

FIGURE 2. Microphotographs of the original and thermally treated samples under the microscope of reflecting (a−d) and fluorescent (e−h) modes. (a) Semifusinite and vitrinite in XFL2. (b) Fusinite with high reflectance (center) and vitrinite with low reflectance in XFL4. (c) Fusinite with irregular dark-colored pores in XFL6. (d) Fusinite with high reflectance in XFL7. (e) Bright orange fluorescence at the edges of vitrinite in XFL0. (f) Orange fluorescence at the edges of vitrinite in XFL1. (g) Weak fluorescent edges of the macerals in XFL3. (h) No fluorescence of the macerals in the XFL4.

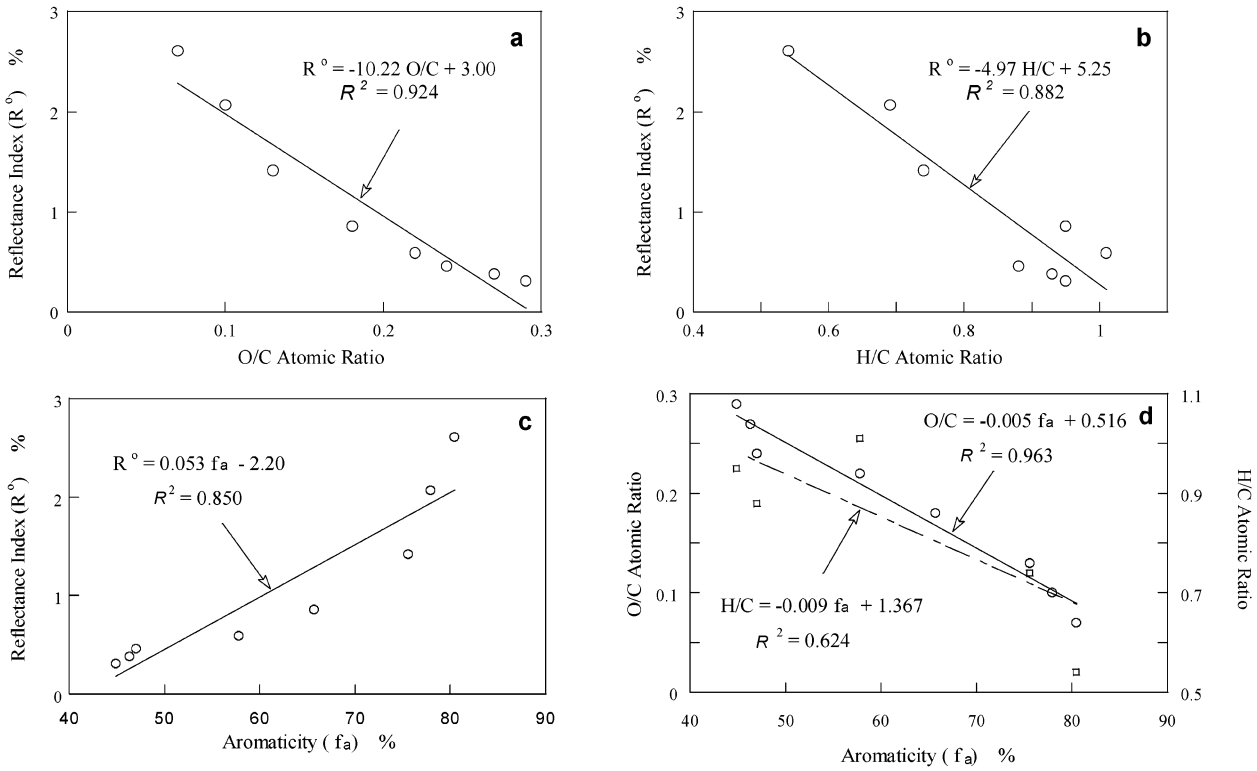

FIGURE 3. Intercorrelations among reflectance index (R^0), atomic ratios, and aromaticity (f_a) for the eight kerogen samples.

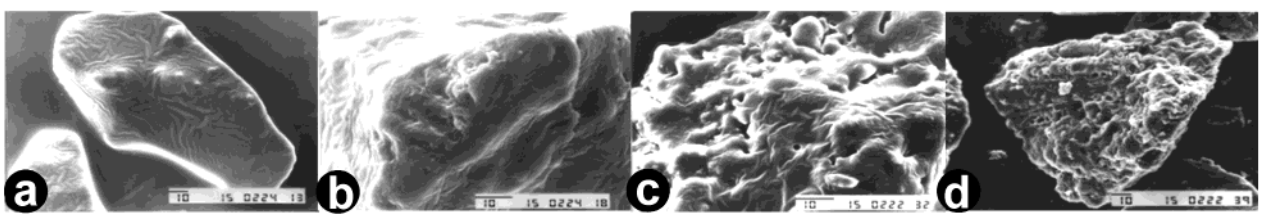

FIGURE 4. Scanning electron microscopic photographs. (a) Original lignite (XFL0) with smooth surface. (b) Lignite treated at 250 °C (XFL2) showing slightly altered surfaces. (c) Lignite treated at 400 °C (XFL5) exhibiting porous surfaces. (d) Lignite treated at 500 °C (XFL7) with highly porous structures.

chains become a fluidal state (*36*, *44*−*46*). Prior studies showed that, upon heating to 300 °C, low-grade coal such as lignite can loosen the compact aliphatic moieties to relatively expanded and amorphous regions (*36*, *44*−*46*), hence lowering the porosity of the organic matter and increasing partitioning of HOCs into the organic matrixes as shown below. As *T* increases, the fluidal aliphatic chains may start to be cracked and removed, and the organic matrixes become more rigid and porous, increasing the bulk porosity and SSA.

^{13}C NMR Spectra. Solid-state ^{13}C NMR spectra measured for the eight solids are shown in Figure 5, and the quantitative analyses of the spectra are summarized in Table SI-1 in the Supporting Information. Both Figure 5 and Table SI-1 show seven major resonance peaks for the original lignite. These peaks can be assigned to aliphatic C (0−45 ppm), methoxyl C (45−63 ppm), carbohydrate C (63−93 ppm), aromatic C (93−148 ppm), oxygen-substituted aromatic C (148−165 ppm), carboxyl C (165−187 ppm), and carbonyl C (187−220 ppm). As treatment temperature increases, the relative peak intensity of the aromatic C increases dramatically from 25.1% for XFL0 and XFL1 to 58.2% for XFL6 and to 62.0% for XFL7 whereas the intensity of the aliphatic C decreases from 33.1% to 33.7 and from 5.1 to 4.99%, respectively. Meanwhile, the relative peak intensity increases from 4.75% to 7.26−12.1% for carbohydrate and from 9.34 to 20.1% for carbonyl C but decreases from 11.7% to 2.28% for oxygen-containing aromatic C and from 7.36% to 0 for methoxyl C and from 8.63% to 0 for carboxyl C.

Table SI-1 shows that the aromaticity calculated from the ^{13}C NMR spectra increases from 44.9−47.0% for XFL0−2 to 57.8% for XFL3, 75.5% for XFL5, and 77.9 and 80.5% for XFL6 and XFL7, respectively. The observed increase of aromaticity as a function of *T* is consistent with the changes of elemental composition and optical properties of the samples. Figure 3c,d shows that the aromaticitiy correlates nearly linearly with H/C and O/C atomic ratios and reflectance index, indicating that kerogen becomes structurally more aromatic, chemically more reduced, and physically more rigid as thermal alterations increase.

FT-IR Spectra. The change of organic functionalities among the eight samples is also well-documented in the FTIR spectra shown in Figure 6. According to the peak assignments of FTIR spectra (Table SI-2), the O−H stretching vibration of carboxylic C at 3400 cm^{-1} and the C═O stretching vibration of carboxylic C at 1700 cm^{-1}decrease from XFL0 to XFL3 and disappear in XFL4, consistent with the observations from ^{13}C NMR spectra. The C−H stretching vibration of aliphatic C at 2980 cm^{-1} and the C−H bending of branched aliphatic C at 1400 cm^{-1} vary slightly in XFL0−2, and both decrease rapidly from XFL3 and finally disappear in XFL5−7. These spectroscopic properties indicate a transition from decarboxylation reactions to C−C cracking at T ∼300 °C. Conversely, the C═C stretching vibration of aromatic C at

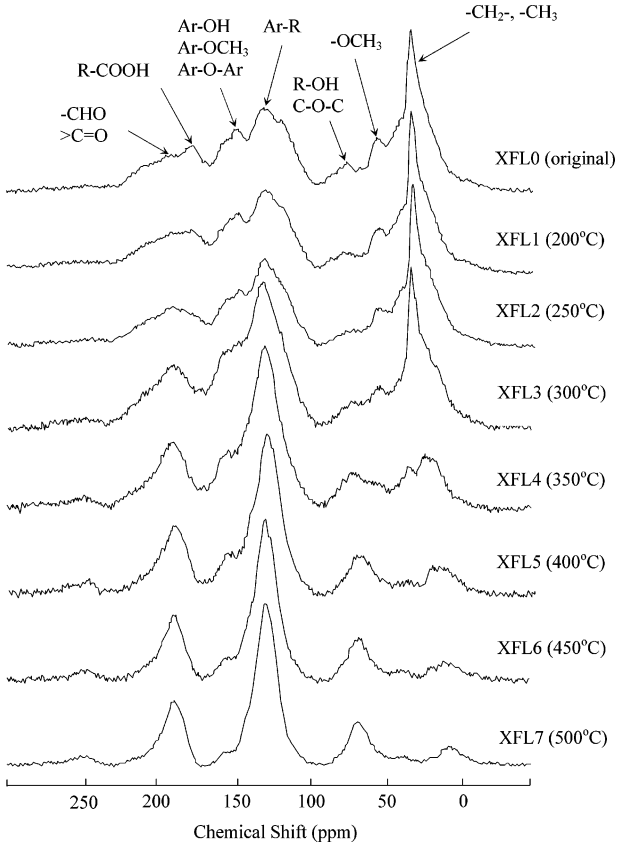

FIGURE 5. CP/MAS ^{13}C NMR spectra of the eight kerogen samples.

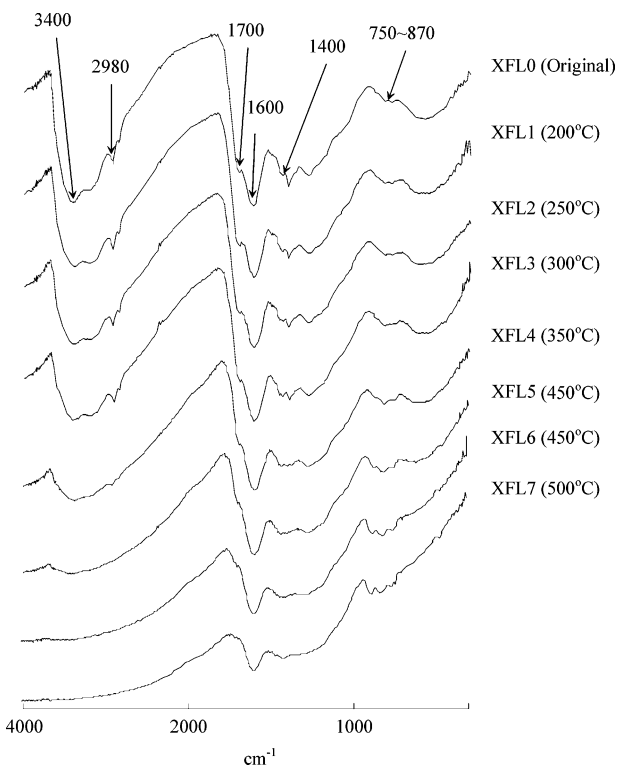

FIGURE 6. FTIR spectra of the eight kerogen samples.

1600 cm^{-1} and the C−H bending vibration of aromatic C at 750, 820, and 860 cm^{-1} are more pronounced as T increases. This appears consistent with the increased aromaticity, higher contents of unsubstituted aromatic carbon, and lower contents of substituted C on aromatic rings due to thermal treatment.

Isotherm Data Reduction. The isotherm model for reducing the equilibrium sorption data obtained for phenanthrene and TCB is the Freundlich model having the following forms:

$$q_e = K_F C_e^{\,n} \tag{1}$$

or

$$\log q_e = \log K_F + n \log C_e \tag{2}$$

where C_e (μg/L) and q_e (μg/g) are aqueous-phase and solid-phase equilibrium solute concentrations, respectively, and K_F [(μg/g)/(μg/L)^n] and n are the Freundlich sorption capacity parameter and isotherm linearity index, respectively. A linear regression procedure using SYSTAT software (Version 10.0, SYSTAT Inc.) was utilized for fitting eq 2 to the logarithmically transformed sorption and desorption data. The resulting log K_F and n parameter values along with their standard deviations, number of observations, and R^2 value are given in Table 2. Phenanthrene sorption and desorption isotherm data measured for the eight kerogen samples along with their best-fit Freundlich isotherms and the model parameters are shown in Figure 7. The sorption and desorption isotherms measured for TCB are shown in Figure SI-1 in the Supporting Information. For better comparison, the best-fit phenanthrene sorption isotherms for the eight sorbents were plotted in Figure 8.

The apparent sorption−desorption hysteresis was quantified using a hysteresis index (HI) defined below (*9*, *43*):

$$\mathrm{HI} = \frac{q_e^{\,d} - q_e^{\,s}}{q_e^{\,s}}\Big|_{T,C_e} \tag{3}$$

where $q_e^{\,s}$ and $q_e^{\,d}$ are solid-phase solute concentrations computed from the best-fit Freundlich model parameters listed in Table 2 for sorption and desorption isotherms, respectively, and the subscripts T and C_e specify constant conditions of temperature and residual solution-phase concentration, respectively. HI values at 22 °C and three different concentration levels were calculated, and the results are included in Table 2.

Sorption and Desorption Isotherms and Apparent Hysteresis. The results presented in Table 2 and Figures 7, 8, and SI-1 indicate that the characteristics of sorption−desorption isotherms are highly affected by the thermal history of the kerogen samples and hence are correlated well with the physicochemical properties of the kerogen. For a given solute tested, the sorption isotherm becomes increasingly more nonlinear as T increases. Table 2 and Figure 7 demonstrate that the phenanthrene sorption isotherm linearity (n) decreases from 0.65 for XFL0 to 0.64 for XFL1 and to 0.24 for XFL7. Figure 9 shows that the phenanthrene sorption isotherm linearity (n) is proportional to the H/C and O/C atomic ratios and is inversely correlated with the R^0 and f_a values of the kerogen matrix. Regressions of the n values of both phenanthrene and TCB isotherms against R^0, f_a, and the H/C and O/C atomic ratios result in fairly linear correlations (Figure 9 and Table 3). These linear intercorrelations strongly suggest that physically more condensed, chemically more reduced, and structurally more aromatic kerogen matrix exhibits greater isotherm nonlinearity.

Figures 8 shows that the phenanthrene sorption capacity increases initially and then decreases rapidly as T increases. The log K_F value shown in Figure 7 and Table 2 increases from 2.61 for XFL0 to a maximum value of 3.24 for XFL4 and then decreases to 2.77 for XFL7. The change of the phenanthrene sorption capacity as a function of T is best illustrated by temperature-dependent single-point K_{OC} values at C_e =

TABLE 2. Sorption and Desorption Isotherm Parameters, Single-Point K_{OC} Values, and Apparent Sorption−Desorption Hysteresis

Phenanthrene

	Freundlich model parameters for sorption							Desorption				Hysteresis Index (HI) at C_e=		
					K_{oc} (L/g)[c] at C_e =									
sample	log K_F[a]	n	R^2	N[b]	5 μg/L	50 μg/L	500 μg/L	log K_F	n	R^2	N	5 μg/L	50 μg/L	500 μg/L
XFL0	2.606 (0.020)[g]	0.651 (0.010)[h]	0.996	19	381	171	76	2.652 (0.023)	0.678 (0.014)	0.992	19	0.16	0.24	0.31
XFL1	2.792 (0.021)	0.637 (0.010)	0.995	20	554	240	104	2.945 (0.022)	0.618 (0.014)	0.990	20	0.38	0.32	0.26
XFL2	2.896 (0.021)	0.629 (0.011)	0.995	20	673	287	122	2.900 (0.023)	0.677 (0.015)	0.991	20	0.09	0.22	0.36
XFL3	3.190 (0.015)	0.576 (0.008)	0.996	20	1197	451	170	3.291 (0.016)	0.572 (0.011)	0.993	20	0.25	0.24	0.23
XFL4	3.235 (0.017)	0.493 (0.009)	0.994	20	1087	338	105	3.406 (0.013)	0.524 (0.010)	0.994	20	0.56	0.67	0.80
XFL5	2.840 (0.020)	0.391 (0.012)	0.986	18	346	85	21	2.977 (0.007)	0.455 (0.007)	0.997	18	0.52	0.76	1.04
XFL6	2.636 (0.016)	0.304 (0.009)	0.986	20	181	37	7	2.703 (0.010)	0.346 (0.008)	0.990	20	0.25	0.38	0.51
XFL7	2.764 (0.014)	0.240 (0.008)	0.986	16	211	37	6	2.783 (0.014)	0.315 (0.012)	0.981	16	0.18	0.40	0.67

1,3,5-Trichlorobenzene

	Freundlich model parameters for sorption							Desorption				Hysteresis Index (HI) at C_e=		
					K_{oc} (L/g)[c] at C_e =									
sample	log K_F[a]	n	R^2	N[b]	10 μg/L	100 μg/L	1000 μg/L	log K_F	n	R^2	N	10 μg/L	100 μg/L	1000 μg/L
XFL0	1.435 (0.043)	0.786 (0.021)	0.994	10	28	17	10	1.616 (0.047)	0.680 (0.023)	0.992	9	0.48	0.16	-[i]
XFL1	1.675 (0.015)	0.762 (0.007)	0.999	10	44	25	15	1.799 (0.029)	0.684 (0.015)	0.997	9	0.38	0.16	-
XFL3	2.277 (0.033)	0.701 (0.017)	0.996	10	145	73	37	2.396 (0.044)	0.641 (0.023)	0.991	9	0.47	0.28	0.11
XFL5	2.326 (0.030)	0.579 (0.015)	0.995	10	107	41	15	2.606 (0.032)	0.566 (0.019)	0.993	8	1.50	1.42	1.35
XFL7	2.151 (0.034)	0.468 (0.015)	0.992	10	51	15	4	2.562 (0.017)	0.503 (0.012)	0.997	8	2.90	3.30	3.60

[a] Units in (μg/g)/(μg/L)^n. [b] Number of observations. [c] Calculated using the listed Freundlich isotherm parameters and the total organic carbon contents listed in Table 1. [d] Units in (μg/g)/(μg/L) or (L/g). [e] Units in (μg/g). [f] Units in (L/μg). [g] One standard deviation of log K_F. [h] ±1 SD of n. [i] Not calculated.

5, 50, and 500 μg/L calculated from the same set of the sorption isotherm parameters. According to Table 2, the single-point K_{OC} value of phenanthrene at C_e = 5 μg/L increases from 381 for XFL0 to 554 for XFL1 and to a maximal value of 1197 for XFL3. It then decreases to 1087 for XFL4 and to 211 for XFL7. Similar trends can be found for K_{OC} values at C_e = 50 and 500 μg/L of phenanthrene, but the K_{OC} value decreases as a function of C_e for the same kerogen due to the nonlinearity of sorption isotherm.

The sorption equilibria measured for TCB exhibit similar characteristics described for phenanthrene. However, for a given sorbent, the TCB sorption isotherm has relatively greater n value and lower sorption capacity then phenanthrene, likely due to the greater aqueous solubility of TCB. As shown in Table 2 and Figure SI-1, the n value for TCB decreases from 0.79 for XFL0 to 0.76 for XFL1 and to 0.47 for XFL7, whereas the log K_F value of TCB increases from 1.44 for XFL0 to 2.33 for XFL5 and then decreases slightly to 2.15 for XFL7. Similarly, the TCB K_{OC} value calculated at C_e = 10 μg/L increases from 28 for XFL0 to 44 for XFL1 and to a maximal value of 145 for XFL3 and finally decreases to 51 for XFL7.

The apparent sorption−desorption hysteresis measured for the two sorbates increases as T increases. As shown in Figures 7, 9, and SI-1, the differences in capacity and nonlinearity between sorption and desorption isotherms are statistically less significant for the original lignite and the sorbents treated at lower temperature, but they are much greater for the sorbents treated at higher temperature conditions. The HI values calculated for phenanthrene at C_e = 500 μg/L increase generally from below 0.4 for XFL0−3 to above 0.5 for XFL4−7 whereas the values calculated for TCB at C_e = 100 μg/L increase from below 0.3 for XFL0−3 to above 1.0 for XFL5−7.

It should be noted that several recent studies reported phenanthrene sorption data for coal, charcoal, and soot and that our data are comparable to some of these studies. LeBoeuf and Weber (*48*) reported n values of 0.62 and 0.57 for the phenanthrene sorption isotherms measured for two low-grade coal samples. The apparent sorption−desorption hysteresis was measurable (0.17−0.48) in their systems, and the calculated HI indices are comparable to the data listed in Table 2 for XFL0−2. Kleineidam et al. (*53*) found that the phenanthrene K_{OC} value increases generally as the grade of coal increases from lignite to sub-bituminous coal and to high-volatile bituminous coal whereas the n values of the phenanthrene sorption isotherms are 0.67, 0.79, and 0.59, respectively. They also reported a charcoal sample with SSA of 220 m^2/g had more nonlinear phenanthrene isotherm (n = 0.58) with higher sorption capacity than their coal samples. Bucheli and Gustafsson (*54*) reported that the phenanthrene K_{OC} values at C_e = 1 μg/L are about 500 L/g for a diesel soot with particle sizes of 180 nm and N_2-BET SSA of 48 m^2/g and that the phenanthrene sorption isotherms are nearly linear (n = 0.87−1). The high n value reported may be due to the narrow C_e range (3−12 μg/L) examined.

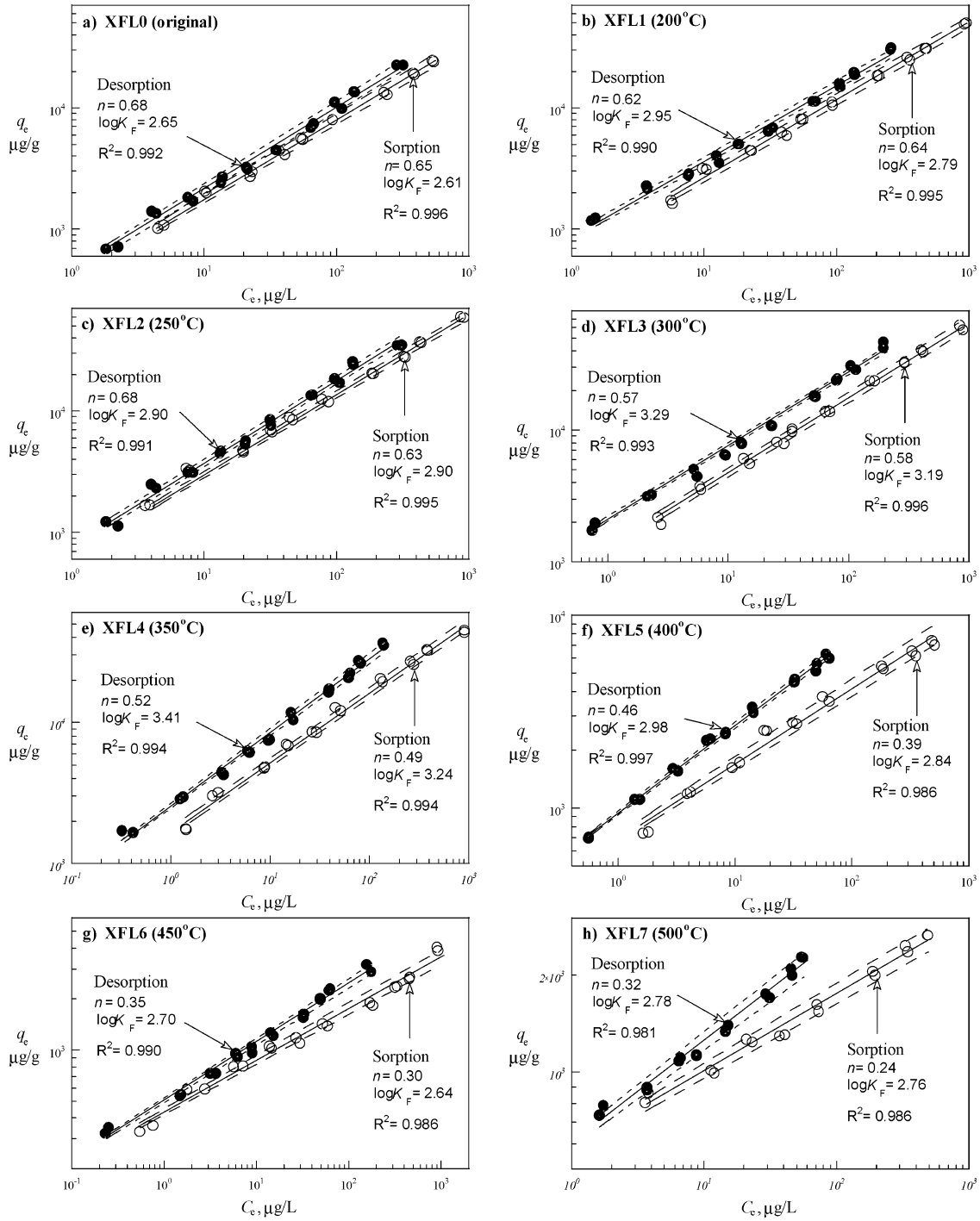

FIGURE 7. Phenanthrene sorption and desorption isotherms measured for the eight kerogen samples. The empty and filled circles represent the measured sorption and desorption data, respectively. The solid lines are the best fits of the data to the Freundlich isotherm model, and the dashed lines represent the best fit isotherms ±1 SD of log K_F and *n* values.

The higher phenanthrene sorption capacities reported in these two studies (*53, 54*) for charcoals and black carbon are likely because the sorbents materials are finer with greater SSA and/or because the sorption equilibria were measured at much lower and narrower C_e ranges. Other studies as summarized in ref *55* reported single-point sorption distribution coefficients that are not readily comparable with our data. For example, Jonker and Koelmans (*20*) measured single-point phenanthrene sorption coefficients for 10 sorbents including soot, coal, charcoal, and activated carbon in the presence of other five PAHs (e.g., pyrene and anthracene) having greater K_{OW} values. Because of the expected nonlinear and strong competitive sorption for these sorbent−sorbate systems, the single-point K_{OC} value could vary over an order of magnitude.

The observed correlations among isotherm nonlinearity, sorption−desorption hysteresis, and sorbent properties are generally consistent with prior studies (*4*−*6, 9, 28*). Grathwohl (*6*) reported that the log K_{OC} value of TCE measured for a set of natural organic materials including three coals and two shales increases as a function of logarithmic H/O atomic ratio of the tested sorbents. Huang and Weber (*9*) reported that the *n* value of the phenanthrene sorption isotherms increases as a function of the O/C atomic ratio of natural organic matter including kerogen and humic acids whereas the HI value decreases accordingly. Nevertheless, these prior

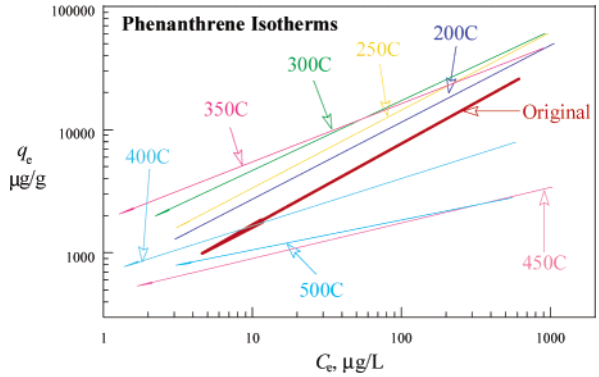

FIGURE 8. Best-fit phenanthrene sorption isotherms for the eight kerogen samples.

studies used sorbents naturally aged from different parental materials, yielding lower R^2 values for their reported correlations.

It should be noted that the observed changes of sorption capacities for both TCB and phenanthrene as a function of sorbent properties are not entirely consistent with prior studies. Huang and Weber (*9*) found that the single-point phenanthrene K_{OC} value at a given C_e increases as the O/C atomic ratio decreases. This finding is consistent only with our observations for the less matured kerogen samples (i.e., XFL0−4). For the more matured samples (i.e., XFL5−7), an opposite trend is observed; i.e., the sorption capacity decreases as the O/C atomic ratio decreases. Apparently, the samples selected in the prior study are possibly less matured, and the observed sorption phenomena are therefore unlikely representative of the kerogen that has undergone more severe alterations.

Mechanistic Interpretations. Table 4 summarizes the major physical and chemical properties observed and quantified for the kerogen samples and the characteristics of the sorption isotherms. The observed sorption and desorption phenomena and their correlations with sorbent properties can be explained using a dual-mode model proposed and applied recently (*8, 10, 47−52*). It is known in kerogen geochemistry literature that the organic matrixes of coals consist mainly of both structurally flexible aliphatic moieties and physically rigid aromatic backbones. The aliphatic moieties are possibly coiled long chains of alkanes and alkenes chemically bonded to aromatic ring structures of the organic matrixes. The rigid aromatic backbones are three-dimensional structures of aromatic sheets held via van der Waals forces, H-bonding, or connected via shared aliphatic branches. The interlayers of aromatic sheets within kerogen matrixes are expandable if they are connected by shared aliphatic branches. The relative content of the two structurally different organic domains depends on the source and relative maturation of the coal. For kerogen having similar source material, the content of aliphatic domain decreases as a function of the degree of organic matrix maturation or as a function of T at which kerogen underwent diagenesis and catagenesis. As T increases, the organic matrixes become more matured as evidenced by systematic changes of physicochemical properties of the sorbents tested in this

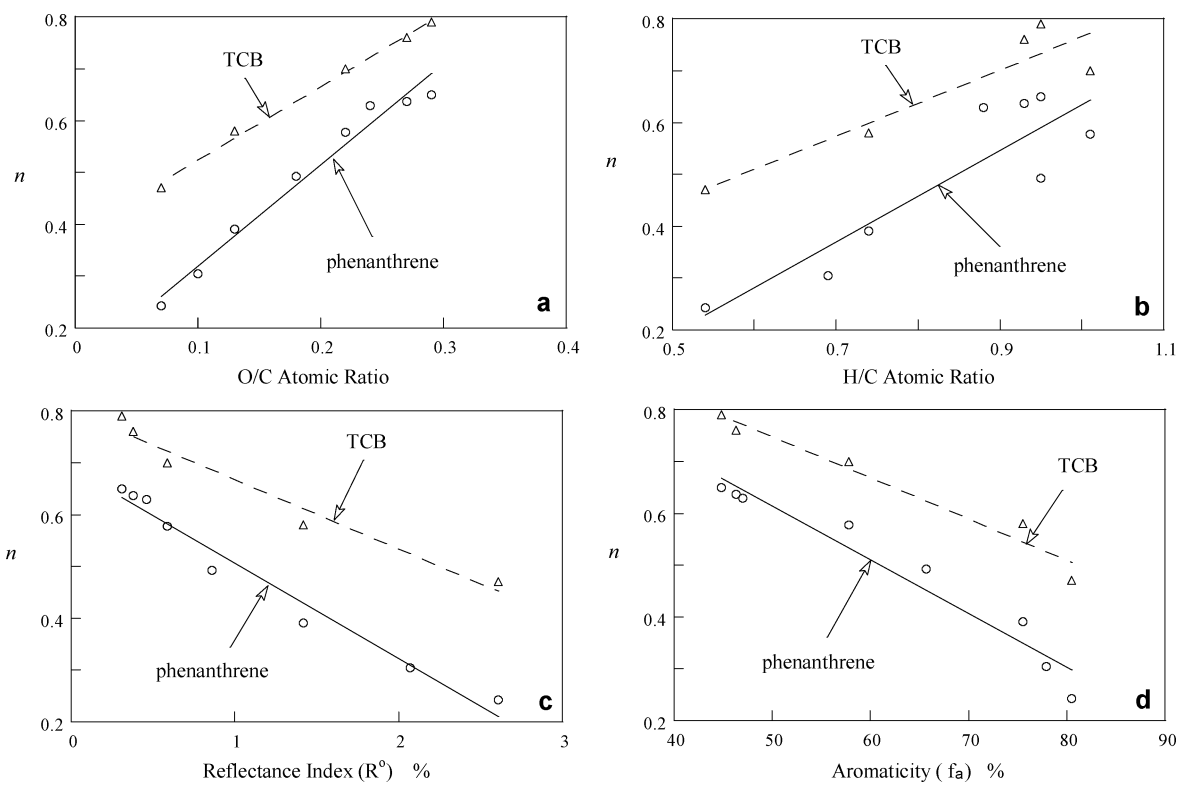

FIGURE 9. Intercorrelations between the isotherm linearity *n* parameter and the physicochemical properties of the kerogen matrixes.

TABLE 3. Best-Fit Intercorrelations between Isotherm Linearity and Selected Sorbent Properties

sorbent property	phenanthrene	TCB
O/C atomic ratio	$n = 1.95\text{O/C} + 0.12$ ($R^2 = 0.974$)	$n = 1.42\text{O/C} + 0.38$ ($R^2 = 0.995$)
H/C atomic ratio	$n = 0.88\text{H/C} - 0.25$ ($R^2 = 0.803$)	$n = 0.64\text{H/C} + 0.13$ ($R^2 = 0.855$)
reflectance index (R^0)	$n = -0.18R^0 + 0.69$ ($R^2 = 0.971$)	$n = -0.13R^0 + 0.80$ ($R^2 = 0.961$)
aromaticity (f_a)	$n = -0.010f_a + 1.135$ ($R^2 = 0.946$)	$n = -0.008f_a + 1.145$ ($R^2 = 0.986$)

TABLE 4. Intercorrelations among Degree of Alterations, Physicochemical Properties, and Sorption Equilibrium Characteristics

Geological Processes	Early Diagenesis	Late Diagenesis	Catagenesis	Early Metagenesis
Tested Samples	XFL0-XFL3	XFL4	XFL5	XFL6, XFL7
Thermal Conditions	T <350°C	300°C< T < 400°C	350°C< T < 450°C	T > 400°C
Dominant Reactions	Decarboxylation	C-C Cracking (long chains)	C-C Cracking (short chains)	Graphitization or charring
Major Properties				
Reflectance Index R°	<0.5 - 0.6%	~0.6% -1.1%	1.1% - ~2%	>~2%
Fluorescence	Yellow, Orange, Brown	Colorless	No Fluorescence	No Fluorescence
Aromaticity	Increasing →			
O/C Atomic Ratio	Decreasing →			
H/C Atomic Ratio	Decreasing →			
Black Carbon Content	Not Detected	Not Detected	Not Detected	>77%
Sorption Isotherm				
Linearity n	Decreasing →			
K_{oc} at referenced C_e	Increasing	Leveling off	Decreasing	Decreasing
Possible Sorption Processes				
Partitioning in aliphatic moieties	Dominating	Dominating	Less significant	Insignificant
Adsorption in expandable aromatic interlayer pores	Dominating	Dominating	Significant	Insignificant
Adsorption in fixed pores	Insignificant	Insignificant	Significant	Dominating
Adsorption on external surfaces	Insignificant	Insignificant	Less significant	Significant

study. These include higher reflectance index, less or no transparency, lower energy light emitted under UV radiation, lower O/C and H/C atomic ratios, and greater aromaticity. The flexibility and expandability of aromatic sheets may decrease as well.

Sorption of less polar and nonpolar organic chemicals by kerogen particles may follow a dual adsorption−partitioning process; nonlinear adsorption on external and internal surfaces of rigid backbones and linear partition into aliphatic mobile moieties. The adsorption process is mechanistically similar to the adsorption of organic chemicals from aqueous solutions to activated carbon or graphitized materials such as charcoal and black carbon whereas the partitioning process might be analogous to the sorption into C18- or C8-based stationary organic phases in a reversed-phase HPLC system. For less matured kerogen, expandable interlayers and high content of aliphatic moeites can accommodate more HOC molecules, exhibiting greater overall sorption capacities. The overall sorption of organic chemicals by kerogen particles is the sum of the adsorption on external and internal surfaces of rigid backbones and partition into aliphatic mobile moieties. A simplest mathematical form of this dual-mode sorption concept is given below (*8, 10, 50, 51*):

$$q_e = K_{D,L}C_e + \frac{Q_a^o bC_e}{1 + bC_e} \quad (4)$$

where $K_{D,L}$ is the distribution or partitioning coefficient of the aliphatic component and b and Q_a^o are respectively the Langmuir site energy and capacity factor for the nonlinear adsorption component. To better illustrate the applicability of the dual-mode model to the sorbent−sorbate systems tested in this study, eq 4 was used to fit the sorption isotherm data. The results are summarized in Table SI-3 in the Supporting Information, and the goodness of fit is shown in Figure 10 for phenanthrene and in Figure SI-2 for TCB.

It is obvious from Figure 10 that the relative contribution of the linear partitioning component to the overall sorption generally decreases as the sorbent treatment temperature increases whereas the relative contribution of the nonlinear adsorption component to the overall sorption increases accordingly. The distribution coefficient of the linear component ($K_{D,L}$) increases from 36.5 for XFL0 to 51.8 for XFL2 and then decreases to 42.2 for XFL3 and finally to 2.8 for XFL7. The capacity parameter Q_a^o increases from 5500 for XFL0 to about 26 000 μg/g for XFL3, and then decreases to about 1400 for XFL7. The site energy parameter b varies within a narrow range of 0.013−0.033 for XFL0−4 and increases rapidly to 0.067 for XFL5 and to 0.3 for XFL7. It is likely that the much faster increase of Q_a^o than $K_{D,L}$ from XFL0 to XFL3 results in decreasing of linearity of the overall sorption isotherm and that the rapid increase of b from XFL4 to XFL7 causes saturation of surface sites at lower C_e, hence further decreases the linearity of the overall sorption isotherm.

The fact that the sorption capacity represented by single-point K_{OC} increases from XFL0 to XFL3 then decreases to XFL7 is likely related to transition from decarboxylation below 250−300 °C to aliphatic carbon chain elimination at higher temperature conditions. As discussed above, at lower temperature conditions, decarboxylation reactions may dominate thermal alterations of the organic matrix, causing rapid decrease of O/C atomic ratio as a function of temperature whereas H/C atomic ratio remains relative constant. The increased hydrophobicity of the organic matrix from XFL0 to XFL3 is apparently consistent with higher sorptive affinity for the tested organic chemicals. As T increases above 250−300 °C, C−C cracking dominates and the aliphatic mobile phase is being eliminated from the aromatic backbones, causing increased aromaticity and lowered H/C atomic ratio. The removal of the aliphatic mobile phase thus results in lowered sorption capacity for the organic pollutants.

Our results indicated that the highly aromatized black carbon generated at 450 (XFL6) and 500 °C (XFL7) exhibits the highest nonlinear sorption isotherms with lowest sorption capacity and the greatest apparent sorption−desorption hysteresis. While the lowered linearity of XFL6 and XFL7 is possibly due to the predominant site-limiting surface adsorption on external and internal rigid carbon matrixes, the lowered sorption capacity likely results from the decreased content of aliphatic carbon moieties that act as a partition

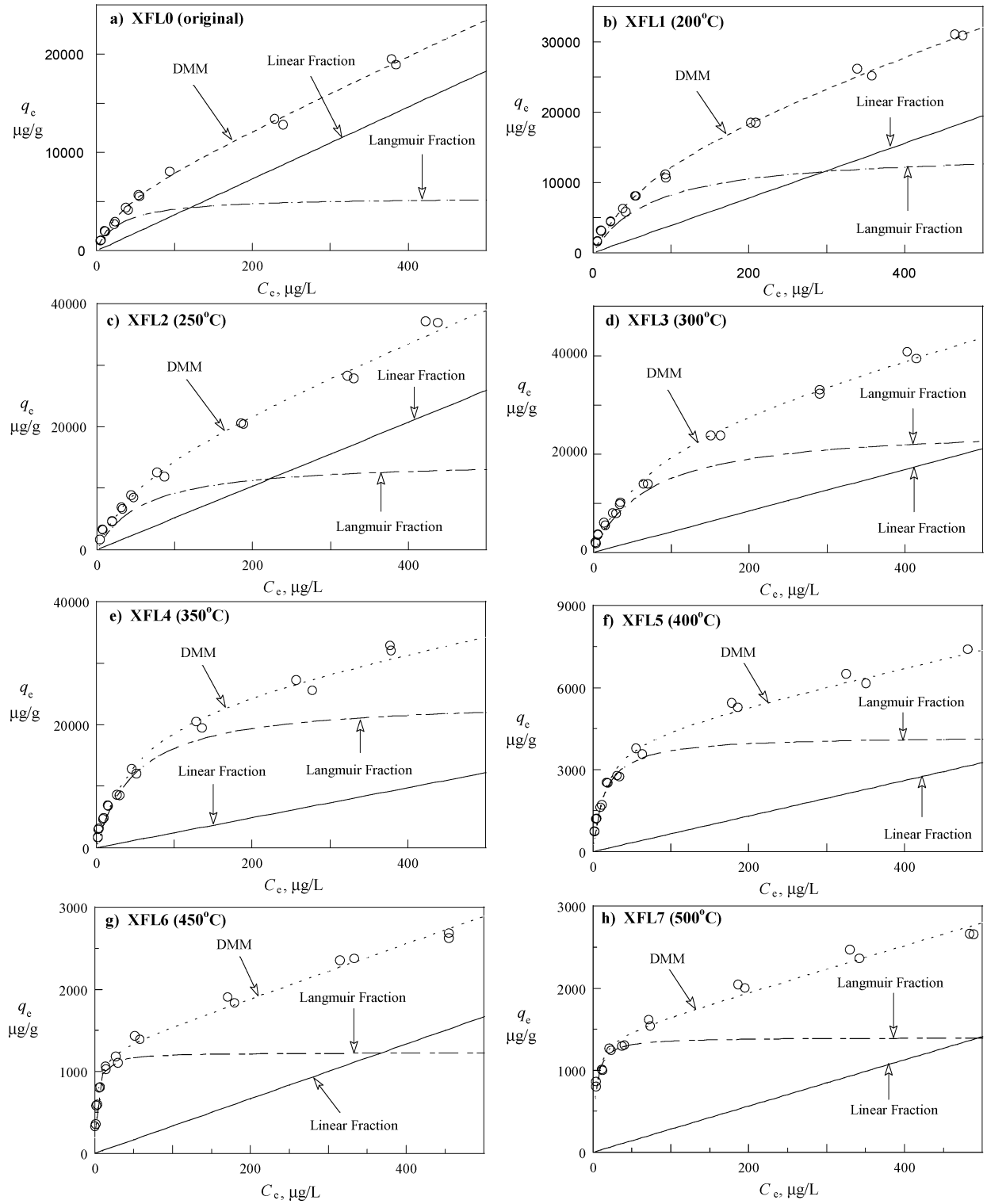

FIGURE 10. Fitting of the phenanthrene sorption data to the dual-mode model for the eight samples. The empty circles are the measured isotherm data. The solid and broken lines represent respectively the contribution of the linear partition and site-limiting adsorption components to the overall sorption (dotted line) of each kerogen sample.

phase for HOCs. This is consistent with a recent study by Chefetz et al. (*56*), which showed pyrene sorption capacity increases as a function of the aliphatic C content of the natural organic matter. Because these two samples have high contents of BC, their sorption capacity is largely depended upon both SSA-related physical properties such as particle sizes, pore volume, and pore size distribution and chemical properties such as their surface functionality and elemental composition.

The positive correlation between the observed apparent sorption−desorption hysteresis (Table 2) and the relative contribution of the adsorption component to the overall sorption (Figure 10 and Table SI-3) indicates that the hysteretic sorption phenomenon may result from solute entrapment within heterogeneous pore structures of the treated organic matrixes. Thermal treatment generated irregularly shaped meso- and micropores within the black carbon matrix. These micropores are hydrophobic in nature

and have very high affinity for hydrophobic solute molecules such as phenanthrene. Once sorbed into these irregularly shaped pores such as ink-bottle shaped pores, sorbate molecules can exhibit significant desorption hysteresis (*9*, *43*, *57*). Hindered intraparticle diffusion of sorbing molecules within pores of sizes slightly greater than the sorbate molecules (*58*) may have enhanced the apparent hysteresis. Jonker and Koelmans (*22*) demonstrated that extraction of tightly bound PAHs from soot and charcoal particles can be complete only when an organic solvent or solvent mixture can swell the BC matrixes, indicating a fraction of PAHs is not readily desorptive in aqueous phase. Braida et al. (*21*) proposed that sorbing molecules (benzene) could deform pore network within charcoal matrixes, causing entrapment of the sorbate and yielding significant sorption−desorption hysteresis.

This study indicated that kerogen materials have varied physicochemical properties due to their different maturation history. The nonlinear and hysteretic sorption and desorption behavior observed for these materials correlates well with their physicochemical properties and hence their maturation history. Kerogen-based coal particles along with black carbon or soot were shown in several recent studies to be important SOM components in topsoils and sediments (*11*−*19*). Because their higher sorption capacity, greater isotherm nonlinearity, and more pronounced desorption hysteresis than humic materials, coal materials are expected to play dominant roles in the overall nonlinear and hysteretic sorption and desorption by bulk soils and sediments and to affect bioavailability and treatability of sediment-bound organic pollutants.

Acknowledgments

We thank Professors Dehan Liu and Jialan Lu of the Guangzhou Institute of Geochemistry, Chinese Academy of Sciences, for their assistance in petrographic examinations and thermal treatment of the sorbent materials, respectively, and Professor Wanzhen Cao of the Center of Organic Analytical Chemistry, the South China University of Technology, for performing the solid-state ^{13}C NMR measurements. This study was funded by U.S. National Science Foundation (BES-011886) and Natural Science Foundation of China (40133010, 40332019 and 40128002).

Supporting Information Available

Figures of sorption and desorption isotherms of TCB and fitting of the Freundlich isotherm model and the dual-mode model to the sorption data. This material is available free of charge via the Internet at http://pubs.acs.org.

Note Added after ASAP Posting

This paper was released ASAP on 07/20/2004 with incorrect units for the Hysteresis Index of phenanthrene in Table 2 and in the paragraph below Table 2. The correct version was posted on 08/12/2004.

Literature Cited

(1) Chiou, C. T.; Peters, L. J.; Freed, V. H. *Science* **1979**, *206*, 831−832.
(2) Karickhoff, S. W. *J. Hydraul. Eng.* **1984**, *110*, 707−735.
(3) Means, J. C.; Wood, S. G.; Hassett, J. J.; Banwart, W. L. *Environ. Sci. Technol.* **1980**, *14*, 1524−1528.
(4) Garbarini, D. R.; Lion, L. W. *Environ. Sci. Technol.* **1986**, *20*, 1263−1269.
(5) Gauthier, T. D.; Seitz, W. R.; Grant, C. L. *Environ. Sci. Technol.* **1987**, *21*, 243−248.
(6) Grathwohl, P. *Environ. Sci. Technol.* **1990**, *24*, 1687−1693.
(7) Weber, W. J., Jr.; McGinley, P. M.; Katz, L. E. *Environ. Sci. Technol.* **1992**, *26*, 1955−1962.
(8) Pignatello, J. J.; Xing, B. *Environ. Sci. Technol.* **1996**, *30*, 1−11.
(9) Huang, W.; Weber, W. J., Jr. *Environ. Sci. Technol.* **1997**, *31*, 2562−2569.
(10) LeBoeuf, E. J.; Weber, W. J., Jr. *Environ. Sci. Technol.* **1997**, *31*, 1697−1702.
(11) Karapanagioti, H. K.; Childs, J.; Sabatini, D. *Environ. Sci. Technol.* **2001**, *35*, 4684−4698.
(12) Accardi-dey, A.; Gschwend, P. M. *Environ. Sci. Technol.* **2002**, *36*, 21−29.
(13) Ran, Y.; Huang, W.; Rao, P. S. C.; Liu, D.; Fu, J.; Sheng, G. *J. Environ. Qual.* **2002**, *31*, 1953−1962.
(14) Song, J.; Peng, P.; Huang, W. *Environ. Sci. Technol.* **2002**, *36*, 3960−3967.
(15) Gustafsson, Ö.; Haghseta, F.; Chan, C.; MacFarlane, J.; Gschwend, P. M. *Environ. Sci. Technol.* **1997**, *31*, 203−209.
(16) Accardi-Dey, A.; Gschwend, P. M. *Environ. Sci. Technol.* **2003**, *37*, 99−106.
(17) Hong, L.; Ghosh, U.; Mahajan, T.; Zare, R. N.; Luthy, R. G. *Environ. Sci. Technol.* **2003**, *37*, 3625−3634.
(18) Naes, K.; Axelman, J.; Naf, C.; Broman, D. *Environ. Sci. Technol.* **1998**, *32*, 1786−1792.
(19) Persson, N. J.; Gustafsson, Ö.; Bucheli, T. D.; Ishaq, R.; Nas, K.; Broman, D. *Environ. Sci. Technol.* **2002**, *36*, 4968−4974.
(20) Jonker, M. T. O.; Koelmans, A. A. *Environ. Sci. Technol.* **2002**, *36*, 3725−3734.
(21) Braida, W. J.; Pignatello, J. J.; Lu, Y.; Ravikovitch, P. I.; Neimark, A. V.; Xing, B. *Environ. Sci. Technol.* **2003**, *37*, 409−417.
(22) Jonker, M. T. O.; Koelmans, A. A. *Environ. Sci. Technol.* **2002**, *36*, 4107−4113.
(23) Hawthorne, S. B.; Miller, D. J. *Environ. Sci. Technol.* **2003**, *37*, 3587−3594.
(24) Huang, W.; Peng, P.; Yu, Z.; Fu, J. *Appl. Geochem.* **2003**, *18*, 995−972.
(25) Ran, Y.; Xiao, B.; Huang, W.; Peng, P.; Liu, D.; Fu, J.; Sheng, G. *J. Environ. Qual.* **2003**, *32*, 1701−1709.
(26) Xiao, B.; Yu, Z.; Peng, P.; Song, J.; Huang, W. *Environ. Sci. Technol.* (submitted for publication).
(27) Huang, W.; Weber, W. J., Jr. *Environ. Sci. Technol.* **1998**, *32*, 3549−3555.
(28) Young, T. M.; Weber, W. J., Jr. *Environ. Sci. Technol.* **1995**, *29*, 92−97.
(29) Kleineidam, S.; Rügner, H.; Ligouis, B.; Grathwohl, P. *Environ. Sci. Technol.* **1999**, *33*, 1637−1644.
(30) Chiou, C. T.; Kile, D. E.; Rutherford, D. W.; Sheng, G.; Boyd, S. A. *Environ. Sci. Technol.* **2000**, *34*, 1254−1258.
(31) Ghosh, U.; Gillette, J.; Luthy, G. R.; Zare, R. N. *Environ. Sci. Technol.* **2000**, *34*, 1729−1736.
(32) Yang, Y.; Sheng, G. *Environ. Sci. Technol.* **2003**, *37*, 3635−3639.
(33) Durand, B. *Kerogen*: *Insoluble Organic Matter from Sedimentary Rocks*; Paris, 1980.
(34) Tissot, B. P.; Welte, D. H. *Petroleum Formation and Occurrence*; Springer-Verlag: New York, 1984.
(35) Stach, E.; Mackowsky, M.-t.; Teichmuller, M.; Taylor, G. H.; Chandra, D.; Teichmuller, R. *Coal Petrology*; Gebruder Borntraeger: Berlin, 1982.
(36) Willams, M.; Vanderborgh, N. E.; Walder, R. D. In *Coal Science and Chemistry*; Volborth, A., Ed.; Elsevier: Amsterdam, 1987; pp 435−459.
(37) Binger, C. A.; Martin, J. P.; Allen-King, R. M.; Fowler, M. *J. Contam. Hydrol.* **1999**, 137−158.
(38) Saxby, J. D.; Riley, K. W. *Nature* **1984**, *308*, 177−179.
(39) Saxby, J. D.; Bennett, A. J. R.; Corcoran, J. F.; Lambert, D. E.; Riley, K. W. *Org. Geochem.* **1986**, *9*, 69−81.
(40) Dunlop, N. F.; Johns, R. B. *Org. Geochem.* **1999**, *30*, 1301−1309.
(41) Xiong, Y.; Geng, A. *Org. Geochem.* **2000**, *31*, 1441−1449.
(42) Wauchope, R. D.; Savage, K. E.; Koskinen, W. C. *Weed Sci.* **1983**, *31*, 744−751.
(43) Huang, W.; Yu, H.; Weber, W. J., Jr. *J. Contam. Hydrol.* **1998**, *31*, 129−148.
(44) Parks, T. J.; Lynch, L. J.; Webster, D. S. *Fuel* **1987**, *66*, 338−344.
(45) Parks, T. J.; Lynch L. J.; Webster, D. S. *Energy Fuels* **1988**, *2*, 185−190.
(46) Maroto-Valer, M. M.; Andresen, J. M.; Snape, C. E. *Fuel* **1997**, *76*, 1301−1308.
(47) LeBoeuf, E. J.; Weber, W. J., Jr. *Environ. Sci. Technol.* **2000**, *34*, 3623−3631.
(48) LeBoeuf, E. J.; Weber, W. J., Jr. *Environ. Sci. Technol.* **2000**, *34*, 3632−3640.
(49) Weber, W. J., Jr.; Huang, W.; LeBoeuf, E. *J. Colloids Surf. A* **1999**, *151*, 167−179.
(50) Xing, B.; Pignatello, J. J.; Gigliotti, B. *Environ. Sci. Technol.* **1996**, *30*, 2432−2440.
(51) Huang, W.; Schlautman, M. A.; Weber, W. J., Jr. *Environ. Sci. Technol.* **1996**, *30*, 2993−3000.

(52) Weber, W. J., Jr.; LeBoeuf, E. J.; Young, T. M.; Huang, W. *Water Res.* **2001**, *35*, 853−868.
(53) Kleineidam, S.; Schüth, C.; Grathwohl, P. *Environ. Sci. Technol.* **2002**, *36*, 4689−4697.
(54) Bucheli, T. D.; Gustafsson, Ö. *Environ. Sci. Technol.* **2000**, *34*, 5144−5151.
(55) Cornelissen, G.; Gustafsson, Ö. *Environ. Sci. Technol.* **2004**, *38*, 148−155.
(56) Chefetz, B.; Deshmukh, A.; Hatcher, P. G.; Guthrie, E. A. *Environ. Sci. Technol.* **2000**, *34*, 2925−2930.
(57) Gregg, S. J.; Sing, K. S. W. *Adsorption, Surface Area and Porosity*; Academic Press: London, 1982.
(58) Farrell, J.; Reinhard, M. *Environ. Sci. Technol.* **1994**, *28*, 63−72.

Received for review September 19, 2003. Revised manuscript received May 5, 2004. Accepted June 2, 2004.

ES0350381